



CHORUS

This is the accepted manuscript made available via CHORUS. The article has been published as:

Topological spin-hedgehog crystals of a chiral magnet as engineered with magnetic anisotropy

N. Kanazawa, J. S. White, H. M. Rønnow, C. D. Dewhurst, D. Morikawa, K. Shibata, T. Arima, F. Kagawa, A. Tsukazaki, Y. Kozuka, M. Ichikawa, M. Kawasaki, and Y. Tokura

Phys. Rev. B **96**, 220414 — Published 28 December 2017

DOI: [10.1103/PhysRevB.96.220414](https://doi.org/10.1103/PhysRevB.96.220414)

Topological spin-hedgehog crystals of a chiral magnet as engineered with magnetic anisotropy

N. Kanazawa*,¹ J. S. White*,² H. M. Rønnow,³ C. D. Dewhurst,⁴
D. Morikawa,⁵ K. Shibata,⁵ T. Arima,^{5,6} F. Kagawa,⁵ A. Tsukazaki,⁷
Y. Kozuka,¹ M. Ichikawa,¹ M. Kawasaki,^{1,5} and Y. Tokura^{1,5}

¹*Department of Applied Physics, University of Tokyo, Tokyo 113-8656, Japan*

²*Laboratory for Neutron Scattering and Imaging (LNS),*

Paul Scherrer Institute (PSI), CH-5232 Villigen, Switzerland

³*Laboratory for Quantum Magnetism (LQM), Institute of Physics,
École Polytechnique Fédérale de Lausanne (EPFL), CH-1015 Lausanne, Switzerland*

⁴*Institut Laue-Langevin, 6 rue Jules Horowitz 38042 Grenoble, France*

⁵*RIKEN Center for Emergent Matter Science (CEMS), Wako, 351-0198, Japan*

⁶*Department of Advanced Materials Science,*

University of Tokyo, Kashiwa 277-8561, Japan

⁷*Institute for Materials Research, Tohoku University, Sendai 980-8577, Japan*

(Dated: December 11, 2017)

* These two authors equally contributed to this work.

Abstract

We report the engineering of spin-hedgehog crystals in thin films of the chiral magnet MnGe by tailoring the magnetic anisotropy. As evidenced by neutron scattering on films with different thicknesses and with varying magnetic field, we can realize continuously deformable spin-hedgehog crystals, each of which is described as a superposition state of a different set of three spin spirals (a triple- \mathbf{q} state). The directions of the three propagation vectors \mathbf{q} vary systematically, gathering from the three orthogonal $\langle 100 \rangle$ directions towards the film normal as the strength of the uniaxial magnetic anisotropy and/or the magnetic field applied along the film normal increase. The formation of triple- \mathbf{q} states coincides with the onset of topological Hall signals, which is ascribed to skew scattering by emergent magnetic field originating in the non-trivial topology of spin hedgehogs. These findings highlight how nano-engineering of chiral magnets makes possible the rational design of unique topological spin textures.

PACS numbers: 75.25.-j, 75.70.-i, 72.15.Gd

INTRODUCTION

In strongly correlated electron systems, where charge, orbital and spin degrees of freedom are entangled[1], complex magnetic spin patterns are an established source of emergent electromagnetic responses. Examples include multiferroicity in spin spirals[2], the Edelstein effect in spin-momentum-locked systems[3], and the Berry-phase induced Hall effect in non-coplanar spin structures[4]. These emergent phenomena can be characterized by local and/or global geometric quantities, such as a magnetic multipole[5], a toroidal moment[6], and spin chirality[7].

Most notably, topological spin textures generate remarkable and versatile emergent properties, which are relevant also for spintronic applications[8–10]. Owing to the energy cost for unwinding a topological spin arrangement, the spin assembly behaves as a robust superstructural unit and displays strong electromagnetic responses to external stimuli.

Magnetic skyrmions and spin hedgehogs are representative examples, respectively, for two- and three-dimensional topological spin textures[11–16] that generate quantized gauge fluxes acting on electrons. Their topological characteristics are described by an integer winding number $w = \frac{1}{8\pi}\epsilon^{ijk} \int_S dS_k \mathbf{n}(\mathbf{r}) \cdot [\partial_i \mathbf{n}(\mathbf{r}) \times \partial_j \mathbf{n}(\mathbf{r})] = \pm 1$. This quantity describes the mapping of magnetic moments $\mathbf{M}(\mathbf{r})$ from the region of real space S to a sphere of radius the unit vector $\mathbf{n}(\mathbf{r}) = \mathbf{M}(\mathbf{r})/|\mathbf{M}(\mathbf{r})|$; S for the skyrmion and hedgehog are the disk and sphere surrounding the core and the singular point, respectively. Meanwhile, the sensitivity of electrons to the spatial dependence of the relative spin tilting is described by the Berry curvature $b_k = \frac{1}{2}\epsilon^{ijk} \mathbf{n}(\mathbf{r}) \cdot [\partial_i \mathbf{n}(\mathbf{r}) \times \partial_j \mathbf{n}(\mathbf{r})]$, which corresponds to a gauge field, or the so-called emergent magnetic field[7]. The emergent magnetic field affects electrons' motion in the same manner as the classical magnetic field, giving rise to the topological Hall effect[17–19]. As is apparent from the definition of $w = \frac{1}{4\pi} \int_S dS_k b_k$, electrons indeed regard skyrmions and hedgehogs as each having a flux quantum $\pm\phi_0 = \pm h/e$ that emanates from the respective regions S . It is also worth noting that hedgehogs can be viewed as monopoles or anti-monopoles of emergent magnetic field[15, 16, 20].

While topological spin textures are sometimes randomly dispersed as either defects or excited states[15, 21, 22], they can also be densely packed and described in terms of superposition states of spin spirals with propagation vectors \mathbf{q} that define multi- \mathbf{q} states[12, 16, 23–32]. In principle, various multi- \mathbf{q} states are possible by arbitrary choice of ingredient spirals, how-

ever many of them remain unexplored experimentally. In particular, while suggestions for three-dimensional archetypes are scarce, a cubic lattice of topological spin hedgehogs and anti-hedgehogs [Fig.1(c)] formed from a superposition of three orthogonal helices was recently proposed for the chiral-magnet MnGe[16], and directly observed by Lorentz transmission electron microscopy (LTEM)[33]. The latter study provides an important perspective towards resolving the long-standing controversy on the magnetic structure in MnGe from various neutron diffraction studies[34–37].

Magnetic anisotropy can dictate the favorable directions along which spins align, consequently determining both the \mathbf{q} -direction and the propagating pattern (*e.g.*, helical, cycloidal or conical) of spin spirals. Modifying the magnetic anisotropy can also deform a magnetic structure[38] or even cause magnetic phase transitions[39, 40]. Here we investigate the effect of additional magnetic anisotropy imposed on the triple- \mathbf{q} state in MnGe and realize its transformation into a new class of multi- \mathbf{q} states. MnGe thin films with varying uniaxial magnetic anisotropy were prepared by tailoring the film thickness and hence the crystal lattice strain. By measuring directly the \mathbf{q} -vectors of the spin textures using small angle neutron scattering (SANS), the pivotal role of uniaxial anisotropy on the superposition pattern of the spin helices was revealed. In every film, there emerges a triple- \mathbf{q} state, where the \mathbf{q} -vectors are drawn towards the film normal, forming the reciprocal bases for a rhombohedral spin crystal. The mutual angle among \mathbf{q} -vectors continuously decreases according to strength of the uniaxial anisotropy, which enables us to control size of the magnetic unit cell and therefore density of hedgehog-type spin singularities. The mutual angle between \mathbf{q} -vectors is also reduced by an out-of-plane magnetic field H , which consequently induces a transition to the single- \mathbf{q} (conical) state at a H well below the critical field H_c for the ferromagnetic ($\mathbf{q} = \mathbf{0}$) transition. Despite the dilute hedgehogs and weak averaged emergent magnetic field in the thinnest film, non-trivial Hall signals possibly due to topological Hall effect arises, persisting up to the ferromagnetic transition. This may suggest that spin hedgehogs escape from their unwinding even after the disappearance of lattice formation, and their singular emergent field distributions remain as skew scattering centers of conduction electrons.

EXPERIMENTS

MnGe thin films were grown epitaxially along the [111] direction on Si(111) substrates, with micrometer-size crystalline domains forming within the film plane. (See the Supplemental Material for the growth procedure, characterization, and strain estimation[41].) From dark-field TEM images reconstructed using reflection a or b [indicated by the red or blue circle, respectively, in a selected area of the diffraction pattern in Fig. 1(b), right-top panel] we identify two-types of crystalline domains: domains A and B, *i.e.*, bright regions in left and middle panels of Fig. 1(b), respectively, that are related by a mirror operation with respect to the (111) plane (see Ref. [42] for further details).

SANS measurements were performed using the D33 beamline at Institut Laue-Langevin (ILL), Grenoble, France, and the SANS-I and SANS-II instruments at the Swiss Spallation Neutron Source (SINQ), Paul Scherrer Institut (PSI), Switzerland. (See the Supplemental Material for the SANS setup[41].) Since neutron scattering intensity is expected due to the spin textures in both crystalline domains, we illustrate in Fig. 1(d) the expected intensity distribution in reciprocal space on the surface of a sphere of radius q . For the case where the magnetic structure in the thin film is the same as in bulk, *i.e.*, the triple- \mathbf{q} state of three superposed orthogonal spin helices, each of which is fixed along one of $\langle 100 \rangle$ axes [Fig. 1(c)], scattering from each crystal domain produces magnetic Bragg spots aligned with the respective set $\langle 100 \rangle$ directions [white or black spots in Fig. 1(d)]. The total scattering expected [six red spots in Fig. 1(d)] thus displays a six-fold symmetry around the common MnGe[111]/Si[111] axis.

Hall resistivity in the 160-nm-thick film was measured with a conventional four-terminal method by using the AC-transport option of a Physical Property Measurement System (PPMS, Quantum Design). The magnetic field was applied perpendicular to the film plane.

RESULTS AND DISCUSSIONS

Using SANS, we mapped the distribution of \mathbf{q} -vectors describing the three-dimensional spin textures in reciprocal space by performing rocking scans, *i.e.*, measuring the scattering as the sample was rotated by angle ω around the vertical axis [see Fig. 1(a)]. Bearing in mind the model case for bulk MnGe [Fig. 1(d)], we show in Figs. 2(a)-(j) the observed

SANS intensity maps at zero magnetic field for MnGe thin films of various thicknesses [see also Supplemental Material for detailed temperature (T) dependence[41]]. Clear magnetic Bragg spots are identified in each thin film below the helimagnetic ordering temperature T_N (206 K, 204 K and 193 K for 160-nm, 735-nm, 1800-nm-thick films, respectively), which is defined by the peak of magnetization (M) curve as a function of T under a low magnetic field [Figs. 2(c), (g) and (k)]. In each film all \mathbf{q} -vectors are of identical magnitude, and Figs. 2(d), (h) and (l) reveal similar T -variations of $|\mathbf{q}|$ and magnetic modulation period λ ($= 2\pi/q$) for 160-nm, 735-nm, 1800-nm-thick films, respectively. In contrast to the similar T -dependences of $|\mathbf{q}|$, the spot positions and their T variation display a striking dependence on the film thickness. In the 160-nm-thick film, a single spot with \mathbf{q} aligned with the film normal at high temperature splits to form a three-fold spot pattern at low temperature [green shaded region in Figs. 2(c) and (d)]. The appearance of multiple magnetic reflections upon cooling is highly suggestive of the formation of a multi- \mathbf{q} state due to the onset of inter-mode interactions[12, 24, 28]. Such splitting at low temperature into a three-fold spot pattern also occurs in the 735-nm-thick film, with the three regions of scattered intensity each being composed of a two-peak structure, leading to six spots in total. In the 1800-nm-thick film, a six-fold spot pattern is observed in the whole temperature region below T_N . The \mathbf{q} -vectors of the six spots are aligned close to, but not exactly with the $\langle 100 \rangle$ directions expected for bulk MnGe [Fig. 1(d)].

We interpret the non-trivial development of the SANS pattern with both film thickness and temperature in terms of a deformation of the triple- \mathbf{q} structure, not the six- \mathbf{q} structure. Unlike the cubic spin crystal in bulk MnGe, with three orthogonal \mathbf{q} -vectors ($\parallel \langle 100 \rangle$), the triple- \mathbf{q} structures in the films are rhombohedrally distorted with the \mathbf{q} -vectors each aligned closer to the film normal. This observation implies the introduction of a uniaxial magnetic anisotropy of the easy-plane type in the films that is aligned with the film plane. Such anisotropy likely stems from shape anisotropy and/or magneto-crystalline anisotropy, both of which should be stronger in thinner films with larger crystal lattice strain (see Supplemental Material[41]). Figures 3(a) and (b) summarize the observed locations of the magnetic Bragg spots at the lowest T (≈ 2 K) in the three films. By reducing the film thickness and correspondingly increasing strength of the uniaxial magnetic anisotropy, the three \mathbf{q} -vectors of the spin crystal gradually align toward the film normal and trace out different curved trajectories for the two types of crystalline domains [white and black dashed lines in Fig.

3(a)]. The angles θ between the \mathbf{q} -vectors and film normal systematically become larger with increasing thickness, approaching $\theta = \arccos\left(\frac{1}{\sqrt{3}}\right) \approx 54.7^\circ$ expected for the bulk [Fig. 3(b)]. The *curved* trajectories of the three \mathbf{q} -vectors observed on the reciprocal sphere may share a common origin with the magnetic field-driven reorientation process of the spin helix in isostructural MnSi, and which is comprehensively explained by a mean-field theory[43].

To capture topological aspects of the three-dimensional spin structures, in Figs. 3(c)-(h) we illustrate triple- \mathbf{q} spin crystals with different values of $\theta = 10^\circ, 30^\circ$ and 54.7° (the latter describes the cubic spin crystal), and their emergent magnetic field distributions in the magnetic hexagonal unit cell. Triple- \mathbf{q} spin crystals can be generally described using:

$$\mathbf{M}(\mathbf{r}) = \sum_{i=1,2,3} \mathbf{a}_i \cos(\mathbf{q}_i \cdot \mathbf{r}) + \mathbf{b}_i \sin(\mathbf{q}_i \cdot \mathbf{r}),$$

where we consider a three-fold superposition of spin helices around the z -axis using the following: $\mathbf{q}_1 = (\sin \theta, 0, \cos \theta)$, $\mathbf{a}_1 = (\cos \theta, 0, -\sin \theta)$, $\mathbf{b}_1 = (0, 1, 0)$, $\mathbf{q}_2 = \left(-\frac{1}{2} \sin \theta, \frac{\sqrt{3}}{2} \sin \theta, \cos \theta\right)$, $\mathbf{a}_2 = \left(-\frac{1}{2} \cos \theta, \frac{\sqrt{3}}{2} \cos \theta, -\sin \theta\right)$, $\mathbf{b}_2 = \left(-\frac{\sqrt{3}}{2}, -\frac{1}{2}, 0\right)$, $\mathbf{q}_3 = \left(-\frac{1}{2} \sin \theta, -\frac{\sqrt{3}}{2} \sin \theta, \cos \theta\right)$, $\mathbf{a}_3 = \left(-\frac{1}{2} \cos \theta, -\frac{\sqrt{3}}{2} \cos \theta, -\sin \theta\right)$, $\mathbf{b}_3 = \left(\frac{\sqrt{3}}{2}, -\frac{1}{2}, 0\right)$. In each triple- \mathbf{q} state, magnetic moments with positive and negative z -components [red and blue arrows in Figs. 3(c)-(e)] stack periodically along the z -direction. Hedgehog-type topological spin singularities [hedgehog and anti-hedgehog displayed in Figs. 3(j) and (k)] are located where the spin directions flip [Fig. 3(i)]. The emergent magnetic field distributions $b_k = \frac{1}{2} \epsilon^{ijk} \mathbf{n}(\mathbf{r}) \cdot [\partial_i \mathbf{n}(\mathbf{r}) \times \partial_j \mathbf{n}(\mathbf{r})]$ also display singularities, *i.e.*, emergent magnetic monopoles and anti-monopoles [displayed as yellow and green points in Figs. 3(f)-(h)], which connect regions of positive and negative b_z [red and blue regions in Figs. 3(f)-(h)]. By decreasing θ , the magnetic unit cell expands in the x - y plane in proportion to $1/\sin \theta$, while its height along the z -axis converges towards the helical pitch λ . This leads to an increase of the in-plane distance between the hedgehog singularities, while the three-dimensional b -network becomes a two-dimensional array of separated b -pillars [Figs. 3(f) and (g)].

To investigate the emergent electromagnetic responses from the topological spin crystals in the films, we first used SANS to elucidate the magnetic field (H) effect on the rhombohedral spin crystal in the 160 nm thick film. Figures 4(a)-(c) show the development of the scattering maps with H applied along the film normal at $T = 2$ K. The out-of-plane H aligns the three \mathbf{q} -vectors towards the H direction, eventually inducing the transition to a single- \mathbf{q} state around $\mu_0 H = 4$ T, where the spin spiral forms a conical shape. Such a magnetic

transition is observed to occur at $\mu_0 H = 2 - 4$ T at each temperature below 30 K where triple- \mathbf{q} states are clearly discernible in zero H [Fig. 4(f) and see also Supplemental Material for other H -dependence of the distribution of \mathbf{q} -vectors at different temperatures[41]].

Despite the dilute distribution of spin hedgehogs and the faint averaged b in the 160 nm thick film, non-trivial Hall signals arise in the temperature region of the triple- \mathbf{q} state. Figures 4(d) and (e) show the H -dependence of the Hall resistivity ρ_{yx} at various temperatures. At high temperatures above 30 K, ρ_{yx} changes almost proportionally to H up to the ferromagnetic transition at H_c , followed by a gradual variation where the magnetization is nearly aligned (see Supplemental Material for magnetization curves[41]). In contrast, below 30 K the Hall resistivity profile exhibits a broad negative dip structure [yellow shaded regions in Fig. 4(e)], where the triple- \mathbf{q} state forms. As summarized by the color map of the negative contribution to ρ_{yx} [Fig. 4(f)], such dip structures survive above 4 T, *i.e.*, in the nearly single- \mathbf{q} phase. This prevents us from attributing them to the *conventional* topological Hall signals $\rho_{yx}^T \propto b_z$. Instead, we suppose that a different type of topological Hall effect appears in the presence of emergent magnetic field. On the expansion of the magnetic unit cell with H , diffusing spin hedgehogs may become trapped at crystalline defects, magnetic impurity sites, or crystalline domain boundaries, lingering until the full ferromagnetic transition. The strong emergent magnetic fields within the immediate vicinities of dilutely distributed spin hedgehogs may cause skew scatterings of conduction electrons that contribute to the topological Hall signal; it is known that the skew scattering becomes more prominent for a lower density of scattering centers[44]. Here we note that for the thicker films, the existence of micro-cracks at intervals of a few hundreds of nanometers prevents us from performing transport measurements (see Supplemental Material[41]).

CONCLUSIONS

We have revealed by SANS on MnGe thin films that uniaxial magnetic anisotropy controlled by the epitaxial-film thickness modifies the triple- \mathbf{q} hedgehog-anti-hedgehog spin crystal lattice from the cubic to rhombohedral form. A magnetic field can also induce such a rhombohedral deformation, eventually causing the transition into a single- \mathbf{q} conical state. Formation of the three-dimensional spin crystal coincides with the temperature range for non-trivial Hall signals, which do not disappear even in the conical phase. We predict that

inherent spin hedgehogs, which escape from their unwinding even after the conical transition, cause skew scatterings on conduction electrons via their strong emergent magnetic fields. Theoretical investigation of the deformation of the multi- \mathbf{q} states from a multilateral perspective, by considering dipole-dipole interactions, finite-size effects, crystalline strain, and mean-field potential, remain as future challenges as well as experimental measurements of both diffraction and transport properties in variously-sized specimens by micro-fabrication methods.

These results allowed us to demonstrate the pivotal role of magnetic anisotropy in the formation of versatile multi- \mathbf{q} topological spin states. The artificial nano-engineering of the magnetic anisotropy shown here is hence a promising means for expanding the range of topological spin condensates that may generate unique spintronic functionalities based on emergent magnetic fields.

ACKNOWLEDGMENTS

We thank Y. Fujishiro and T. Yokouchi for their fruitful discussions. This work was supported by JSPS KAKENHI (Grants No. 24224009 and No. 15H05456), JST CREST (Grant No. JPMJCR16F1), the Swiss National Science Foundation (SNF) Sinergia network ‘NanoSkyrmionics’, the SNF projects 153451 and 166298, and the European Research Council project CONQUEST. We acknowledge the allocation of neutron beamtime at the Institut Laue Langevin (ILL), Grenoble, France and the Swiss spallation neutron source (SINQ), Paul Scherrer Institute (PSI), Villigen, Switzerland.

-
- [1] M. Imada, A. Fujimori, and Y. Tokura, *Rev. Mod. Phys.* **70**, 1039-1263 (1993).
 - [2] S. Seki and Y. Tokura, *Adv. Mater.* **22**, 1554-1565 (2010).
 - [3] V. M. Edelstein, *Solid State Commun.* **73**, 233-235 (1990).
 - [4] N. Nagaosa, J. Sinova, S. Onoda, A. H. MacDonald, and N. P. Ong, *Rev. Mod. Phys.* **82**, 1539 (2010).
 - [5] L. D. Landau and E. M. Lifshitz, *The Classical Theory of Fields* (Amsterdam: Elsevier, 1980).
 - [6] N. A. Spaldin, M. Fiebig, and M. Mostovoy, *J. Phys.: Condens. Matter* **20**, 434203 (2008).
 - [7] N. Nagaosa and Y. Tokura, *Phys. Scr.* **T146**, 014020 (2012).

- [8] N. Nagaosa, and Y. Tokura, *Nature Nanotechnol.* **8**, 899-911 (2013).
- [9] R. Wiesendanger, *Nat. Rev. Mater.* **1**, 16044 (2016).
- [10] A. Fert, N. Reyren, and V. Cros, *Nat. Rev. Mater.* **2**, 170031 (2017).
- [11] A. N. Bogdanov, and D. A. Yablonskii, *Sov. Phys. JETP* **68**, 101-103 (1989).
- [12] S. Mühlbauer, B. Binz, F. Jonietz, C. Pfleiderer, A. Rosch, A. Neubauer, R. Georgii, and P. Böni, *Science* **323**, 915-919 (2009).
- [13] X. Z. Yu, Y. Onose, N. Kanazawa, J. H. Park, J. H. Han, Y. Matsui, N. Nagaosa, and Y. Tokura, *Nature* **465**, 901-904 (2010).
- [14] E. Feldtkeller, *Z. Angew. Phys.* **19**, 530-536 (1965).
- [15] P. Milde, D. Köhler, J. Seidel, L. M. Eng, A. Bauer, A. Chacon, J. Kindervater, S. Mühlbauer, C. Pfleiderer, S. Buhbrandt, C. Schütte, A. Rosch, *Science* **340**, 1076-1080 (2013).
- [16] N. Kanazawa, Y. Nii, X.-X. Zhang, A. S. Mishchenko, G. De Filippis, F. Kagawa, Y. Iwasa, N. Nagaosa, and Y. Tokura, *Nature Commun.* **7**, 11622 (2016).
- [17] P. Bruno, V. K. Dugaev and M. Taillefumier, *Phys. Rev. Lett.* **93**, 096806 (2004).
- [18] M. Lee, W. Kang, Y. Onose, Y. Tokura, and N. P. Ong, *Phys. Rev. Lett.* **102**, 186601 (2009).
- [19] A. Neubauer, C. Pfleiderer, B. Binz, A. Rosch, R. Ritz, P. G. Niklowitz, and P. Böni, *Phys. Rev. Lett.* **102**, 186602 (2009).
- [20] G. Volovik, *J. Phys. C Solid State Phys.* **20**, L83 (1987).
- [21] C. Castelnovo, R. Moessner, and S. L. Sondhi, *Nature* **451**, 42-45 (2008).
- [22] P. Schoenherr, J. Müller, L. Köhler, A. Rosch, N. Kanazawa, Y. Tokura, M. Garst, and D. Meier, *arXiv:1704.06288* (2017).
- [23] U. K. Rößler, A. N. Bogdanov, and C. Pfleiderer, *Nature* **422**, 797-801 (2006).
- [24] B. Binz, A. Vishwanath, and V. Aji, *Phys. Rev. Lett.* **96**, 207202 (2006).
- [25] S. Tewari, D. Belitz, and T. R. Kirkpatrick, *Phys. Rev. Lett.* **96**, 047207 (2006).
- [26] I. Fischer, N. Shah, and A. Rosch, *Phys. Rev. B* **77**, 024415 (2008).
- [27] S. D. Yi, S. Onoda, N. Nagaosa, and J. H. Han, *Phys. Rev. B* **80**, 054416 (2009).
- [28] S. Heinze, K. von Bergmann, M. Menzel, J. Brede, A. Kubetzka, R. Wiesendanger, G. Bihlmayer, and S. Blgel, *Nature Phys.* **7**, 713-718 (2011).
- [29] S.-Z. Lin, A. Saxena, and C. D. Batista, *Phys. Rev. B* **91**, 224407 (2015).
- [30] S.-G. Yang, Y.-H. Liu, and J. H. Han, *Phys. Rev. B* **94**, 054420 (2016).
- [31] J. P. Chen, D.-W. Zhang, and J.-M. Liu, *Sci. Rep.* **6**, 29126 (2016).

- [32] I. Kézsmárki, S. Bordács, P. Milde, E. Neuber, L. M. Eng, J. S. White, H. M. Rønnow, C. D. Dewhurst, M. Mochizuki, K. Yanai, H. Nakamura, D. Ehlers, V. Tsurkan, and A. Loidl, *Nature Mater.* **14**, 1116-1122 (2015).
- [33] T. Tanigaki, K. Shibata, N. Kanazawa, X. Z. Yu, Y. Onose, H. S. Park, D. Shindo, and Y. Tokura, *Nano Lett.* **15**, 5438-5442 (2015).
- [34] N. Kanazawa, Y. Onose, T. Arima, D. Okuyama, K. Ohoyama, S. Wakimoto, K. Kakurai, S. Ishiwata, and Y. Tokura, *Phys. Rev. Lett.* **106**, 156603 (2011).
- [35] O. L. Makarova, A. V. Tsvyashchenko, G. Andre, F. Porcher, L. N. Fomicheva, N. Rey, and I. Mirebeau, *Phys. Rev. B* **85**, 205205 (2012).
- [36] N. Kanazawa, J.-H. Kim, D. S. Inosov, J. S. White, N. Egetenmeyer, J. L. Gavilano, S. Ishiwata, Y. Onose, T. Arima, B. Keimer, and Y. Tokura, *Phys. Rev. B* **86**, 134425 (2012).
- [37] E. Altynbaev, S.-A. Siegfried, V. Dyadkin, E. Moskvin, D. Menzel, A. Heinemann, C. Dewhurst, L. Fomicheva, A. Tsvyashchenko, and S. Grigoriev, *Phys. Rev. B* **90**, 174420 (2014).
- [38] K. Shibata, J. Iwasaki, N. Kanazawa, S. Aizawa, T. Tanigaki, M. Shirai, T. Nakajima, M. Kubota, M. Kawasaki, H. S. Park, D. Shindo, N. Nagaosa, and Y. Tokura, *Nature Nanotechnol.* **10**, 589-592 (2015).
- [39] E. A. Karhu, U. K. Röbler, A. N. Bogdanov, S. Kahwaji, B. J. Kirby, H. Fritzsche, M. D. Robertson, C. F. Majkrzak, and T. L. Monchesky, *Phys. Rev. B* **85**, 094429 (2012).
- [40] Y. Nii, T. Nakajima, A. Kikkawa, Y. Yamasaki, K. Ohishi, J. Suzuki, Y. Taguchi, T. Arima, Y. Tokura, and Y. Iwasa, *Nature Commun.* **6**, 8539 (2015).
- [41] See Supplemental Material at <http://> for details about growth and characterization of MnGe thin films, temperature and magnetic field dependence of scattering intensity patterns, and magnetization properties in the 160-nm-thick film.
- [42] M. Trabel, N. V. Tarakina, C. Pohl, J. A. Constantino, C. Gould, K. Brunner, and L. W. Molenkamp, *J. Appl. Phys.* **121**, 245310 (2017).
- [43] A. Bauer, A. Chacon, M. Wagner, M. Halder, R. Georgii, A. Rosch, C. Pfleiderer, and M. Garst, *Phys. Rev. B* **95**, 024429 (2017).
- [44] S. Onoda, N. Sugimoto, and N. Nagaosa, *Phys. Rev. B* **77**, 165103 (2008).

Figures

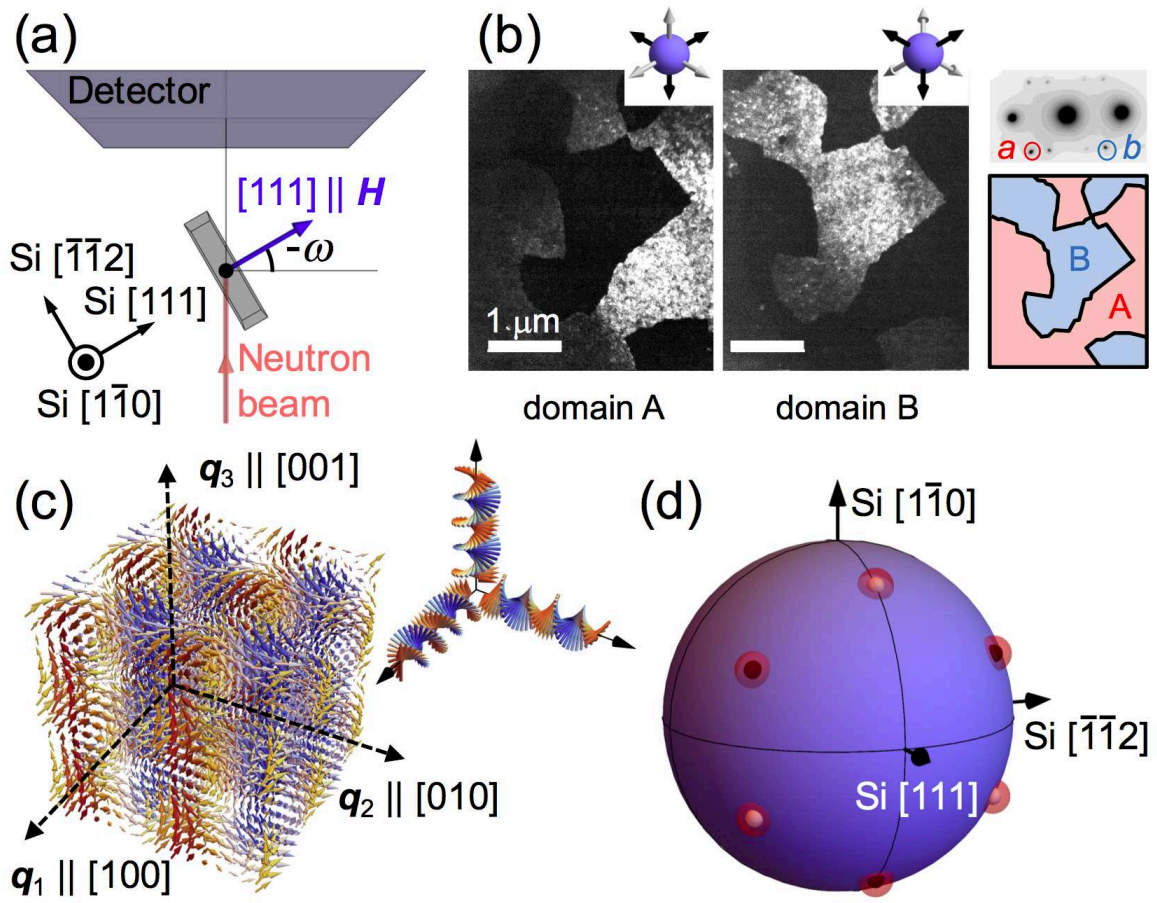


FIG. 1: (a) Schematic illustration of the setup for small-angle neutron scattering. At the rocking angle $\omega = 0^\circ$, the incident neutron beam is parallel to $\text{Si}[\bar{1}\bar{1}2]$ axis. Magnetic field direction is always parallel to $\text{Si}[111]$ axis (the film normal) for rocking scans around the $\text{Si}[1\bar{1}0]$ axis. (b) Dark-field transmission electron microscopy images (left and middle panels) reconstructed using the reflections a or b (right-top panel). The complementary images represent the coexistence of two-types of crystalline domains with different crystalline orientations and chirality, and which are related by mirror operation with respect to (111) plane (right-bottom panel). Here we call them domains A and B, respectively. (c) Schematic illustration of the cubic spin crystal (main panel) formed from superposition of three orthogonal helices (inset), with their propagation vectors \mathbf{q}_i ($i = 1, 2, 3$) parallel to the respective $\langle 100 \rangle$ crystalline axes. (d) Expected neutron scattering intensity map on the surface of a sphere in reciprocal space with constant radius q , and under the assumption that the cubic spin crystal state [panel (c)] is realized in the MnGe thin film with an equal population of the two crystalline domains [panel (b)]. Red dots represent magnetic Bragg reflections, while no scattered intensity is expected in blue part of the sphere. White and black dots represent directions of $\langle 100 \rangle$ crystalline axes of domains A and B, respectively. If the three white dots represent $[100]$, $[010]$ and $[001]$ directions [white arrows in inset of left panel of Fig. 1(b)], the black dots correspond to $[\bar{1}00]$, $[0\bar{1}0]$ and $[00\bar{1}]$ directions [black arrows in inset of middle panel of Fig. 1(b)] due to the mirror operation.

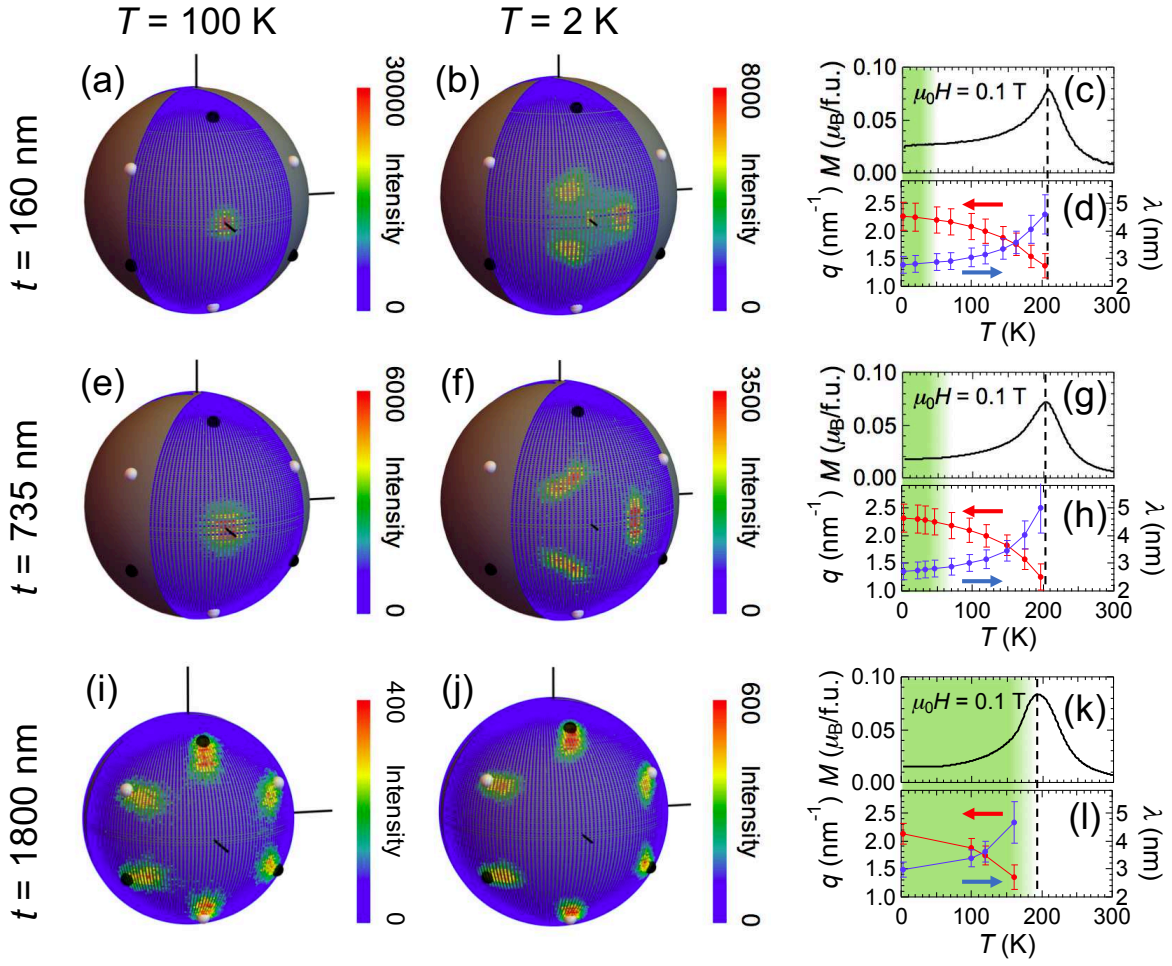


FIG. 2: (a)-(d) Data for the 160-nm-thick film: scattering intensity maps on reciprocal space spheres at high ($T = 100$ K) and low ($T = 2$ K) temperatures [panels (a) and (b)]; T -dependence of the magnetization (M) at $\mu_0 H = 0.1$ T [panel (c)]; and the magnitude of magnetic propagation vector q and magnetic period λ [panel (d)]. (e)-(h) Data set for the 735-nm-thick film. (i)-(l) Data set for the 1800-nm-thick film. Vertical dashed lines on the peaks of M - T curves in panels (c), (d), (g), (h), (k) and (l) indicate the respective helimagnetic ordering temperatures T_N . Green shaded regions in panels (c), (d), (g), (h), (k) and (l) indicate the temperature ranges with formation of the triple- q state.

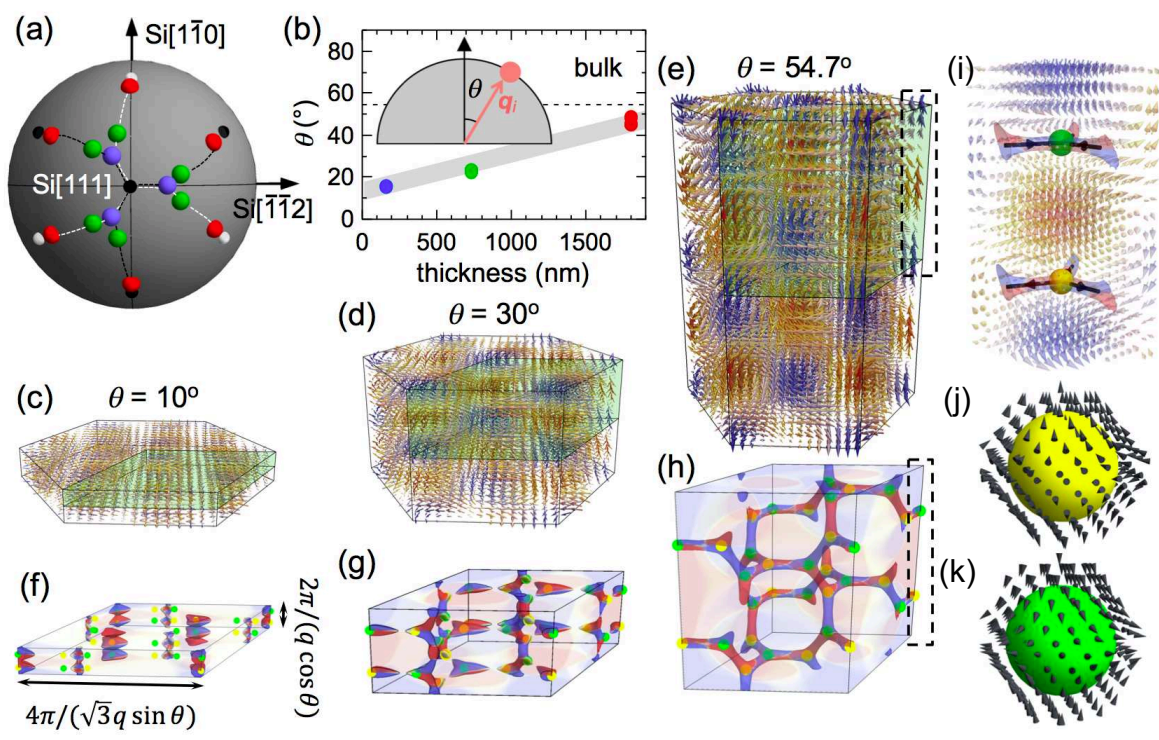


FIG. 3: (a) View along Si[111] of the reciprocal space sphere showing the peak positions of the scattering intensity patterns at $T = 2$ K and $\mu_0 H = 0$ T: blue, green and red spots denote the peaks observed from the 160-nm-, 735-nm- and 1800-nm-thick films, respectively. White and black dots represent the directions of $\langle 100 \rangle$ crystalline axes of the domains A and B, respectively. White and black dashed lines are guides for eye, indicating the trajectories which scattering peak positions follow with changing the uniaxial magnetic anisotropy in the domains A and B, respectively. (b) Thickness dependence of the angle θ between the film normal (MnGe[111] axis) and the \mathbf{q} -vectors. The thick grey line is a guide for the eye. (c)-(e) Schematic illustrations of triple- \mathbf{q} spin states with $\theta = 10^\circ$, 30° and $\arccos(1/\sqrt{3}) \approx 54.7^\circ$ as represented in terms of the hexagonal magnetic cell. Reddish and bluish arrows indicate spins with positive and negative z-components, respectively. (f)-(h) Distributions of hedgehog singularities and emergent magnetic field in the corresponding green box regions of panels (c)-(e). Regions with large magnitude of emergent magnetic field ($|\mathbf{b}| > 0.25, 1.45$ and 4 for triple- \mathbf{q} spin states with $\theta = 0^\circ, 30^\circ$ and 54.7° , respectively) are colored according to the sign of b_z : red and blue for positive and negative b_z , respectively. Relative size scale among the magnetic unit cells is not presented precisely for the purpose of visibility [panels (c)-(h)]. Hedgehog [emergent monopole, panel (j)] and anti-hedgehog [emergent anti-monopole, panel (k)] spin singularities appear where the spin directions flip, *e.g.*, at the midpoints between the red and blue clusters consisting of up- and down-moments as exemplified in panel (i) for the selected region of dashed squares of panels (e) and (h). Black arrows in panel (i) indicate the directions of the large-magnitude emergent magnetic fields.

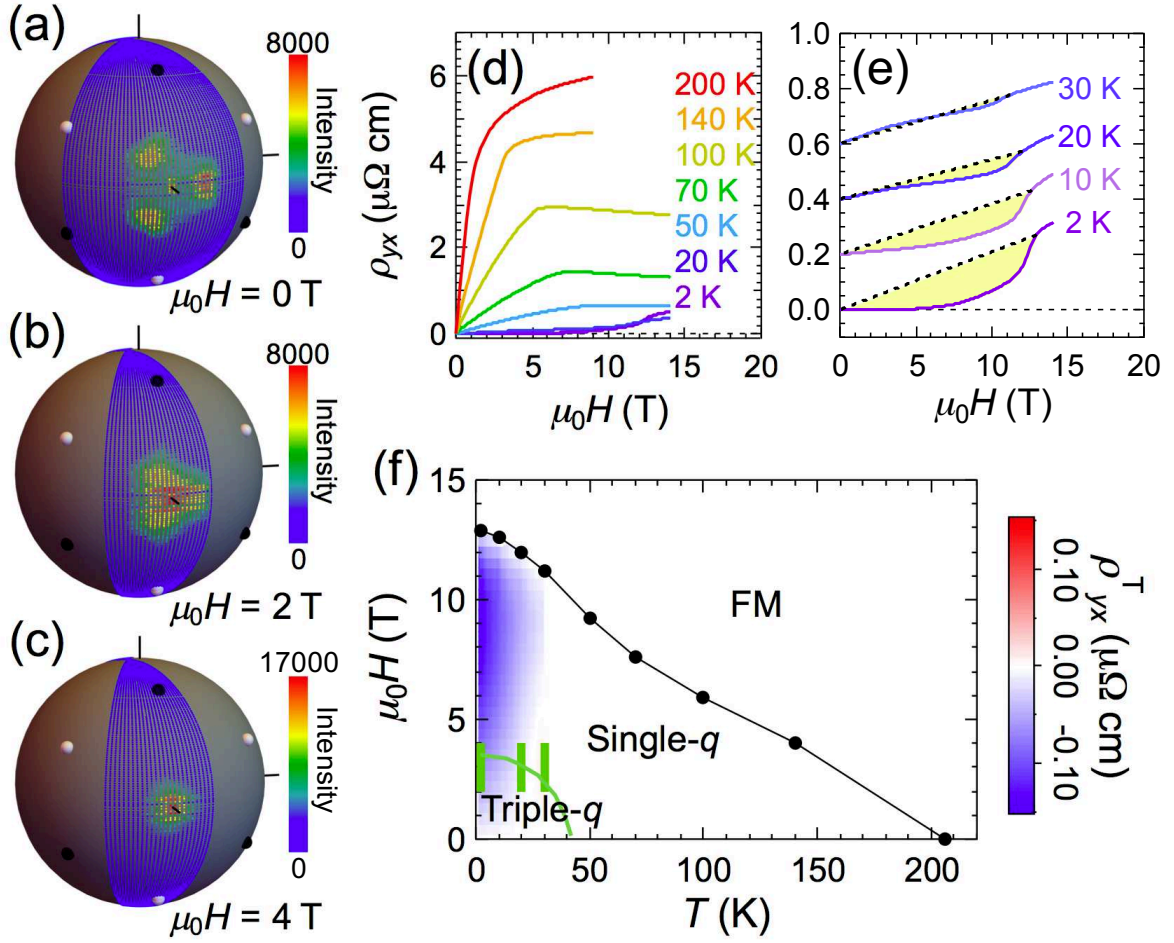


FIG. 4: (a)-(c) Scattering intensity maps on the reciprocal space sphere at $T = 2$ K and $\mu_0 H \parallel \text{MnGe}[111] = 0, 2$ and 4 T. (d) and (e) Hall resistivity at various T . In panel (e) the data are shifted in the vertical direction for visibility. The yellow shaded regions in panel (e) represent estimated non-trivial Hall signals, which are attributed to a topological Hall resistivity ρ_{yx}^T due to skew scatterings by emergent magnetic field. (f) Contour mapping of the non-trivial topological Hall resistivity in the T - $H \parallel \text{MnGe}[111]$ plane. The critical magnetic fields for the ferromagnetic transition H_c [black dots in panel (f)] are defined as inflection points in the ρ_{yx} - H curves. In the low T range, the transition between triple- q and conical states occurs between $\mu_0 H = 2$ – 4 T, as indicated with green thick lines. The green curve is a guide to the eye for the region of the phase diagram that hosts the triple- q state.